Scale-dependent alignment, tumbling and stretching of slender rods in isotropic turbulence

Nimish Pujara[1],†, Greg A. Voth[2] and Evan A. Variano[1]

[1]Department of Civil and Environmental Engineering, University of California, Berkeley, CA 94720, USA

[2]Department of Physics, Wesleyan University, Middletown, CT 06459, USA

We examine the dynamics of slender, rigid rods in direct numerical simulation of isotropic turbulence. The focus is on the statistics of three quantities and how they vary as rod length increases from the dissipation range to the inertial range. These quantities are (i) the steady-state rod alignment with respect to the perceived velocity gradients in the surrounding flow, (ii) the rate of rod reorientation (tumbling) and (iii) the rate at which the rod end points move apart (stretching). Under the approximations of slender-body theory, the rod inertia is neglected and rods are modelled as passive particles in the flow that do not affect the fluid velocity field. We find that the average rod alignment changes qualitatively as rod length increases from the dissipation range to the inertial range. While rods in the dissipation range align most strongly with fluid vorticity, rods in the inertial range align most strongly with the most extensional eigenvector of the perceived strain-rate tensor. For rods in the inertial range, we find that the variance of rod stretching and the variance of rod tumbling both scale as $l^{-4/3}$, where l is the rod length. However, when rod dynamics are compared to two-point fluid velocity statistics (structure functions), we see non-monotonic behaviour in the variance of rod tumbling due to the influence of small-scale fluid motions. Additionally, we find that the skewness of rod stretching does not show scale invariance in the inertial range, in contrast to the skewness of longitudinal fluid velocity increments as predicted by Kolmogorov's 4/5 law. Finally, we examine the power-law scaling exponents of higher-order moments of rod tumbling and rod stretching for rods with lengths in the inertial range and find that they show anomalous scaling. We compare these scaling exponents to predictions from Kolmogorov's refined similarity hypotheses.

Key words: intermittency, isotropic turbulence, particle/fluid flows

1. Introduction

The dynamics of slender rods (or fibres) in turbulence has wide-ranging applications in environmental and industrial processes (for example, see the review by Voth &

† Present address: Department of Civil and Environmental Engineering, University of Wisconsin-Madison, Madison, WI 53706, USA; Email address for correspondence: npujara@wisc.edu

Soldati (2017)). These applications include aerosols in the atmosphere (Newsom & Bruce 1994, 1998; Spurny 2000), textile and paper manufacture (Marheineke & Wegener 2006; Lundell, Söderberg & Alfredsson 2011), the microstructure of clouds and precipitation (Pruppacher & Klett 2012), the scattering of electromagnetic radiation (Alyones & Bruce 2015) and plankton hydrodynamics (Dusenbery 2009; Bordoloi & Variano 2017; Niazi *et al.* 2017). The focus on rods also follows from the fact that they are analytically and numerically tractable using slender-body theory (e.g. Batchelor 1970; Cox 1970; Khayat & Cox 1989; Shin & Koch 2005; Subramanian & Kock 2005; Guazzelli & Hinch 2011; Lopez & Guazzelli 2017).

More generally, the study of rods, discs and triaxial ellipsoids that follow fluid trajectories but rotate in response to local velocity gradients has provided a way to investigate the Lagrangian structure of the smallest scales in turbulence (e.g. Parsa *et al.* 2012; Chevillard & Meneveau 2013; Gustavsson, Einarsson & Mehlig 2014; Ni, Ouellette & Voth 2014; Byron *et al.* 2015; Ni *et al.* 2015; Pujara & Variano 2017). This approach has shown that small rods (or, equivalently, infinitesimal material lines) strongly align with vorticity (Pumir & Wilkinson 2011; Parsa *et al.* 2012), and both rods and vorticity come to align with the Lagrangian fluid stretching direction (Ni *et al.* 2014). Herein, we extend this approach to larger scales and rods that are no longer small enough to follow fluid trajectories. Applications for this include predicting the motion of large anisotropic particles (e.g. Chen, Jin & Zhang 2015; Bordoloi & Variano 2017; Ravnik, Marchioli & Soldati 2017; Pujara *et al.* 2018) and modelling the subgrid-scale stress tensor in large-eddy simulations (e.g. Sreenivasan & Antonia 1997; Meneveau & Katz 2000; He, Rubinstein & Wang 2002; Yang, He & Wang 2008). Studying the dynamics of longer rods also presents an opportunity to further the understanding of inertial-range dynamics of turbulence.

An important feature of the inertial range is internal intermittency (see e.g. Frisch 1995). In the inertial range, there exists a detailed phenomenology of the energy cascade and intermittency, where the majority of intermittency models focus on spatio-temporal variations of a scalar quantity such as the energy dissipation rate or the enstrophy in the spirit of Kolmogorov's refined similarity hypothesis (e.g. Kolmogorov 1962; Oboukhov 1962; Meneveau & Sreenivasan 1991; Chen *et al.* 1997; Nelkin 1999; Donzis, Yeung & Sreenivasan 2008). This assumes that the local average of a single scalar captures the relevant fluctuations in the energy cascade at a given scale and that the structure of the associated fluid motions is not important. However, as we summarise below, recent work on the structure of turbulent flow at scales in the inertial range have provided new insights.

Chertkov, Pumir & Shraiman (1999) introduced the idea of 'tetrad dynamics' where the Lagrangian evolution of four points is studied to understand coarse-grained velocity gradients. This approach of multi-particle statistics has been used to understand the effects of small-scale motions on larger-scale motions and how coarse-grained vorticity aligns in the coarse-grained strain-rate eigenframe (Naso & Pumir 2005; Luthi *et al.* 2007; Xu, Pumir & Bodenschatz 2011; Pumir, Bodenschatz & Xu 2013). Li & Meneveau (2005, 2006) used a heavily simplified model for the Lagrangian evolution of two-point velocity increments derived from the Navier–Stokes equation (the 'advected delta-vee system') to study the origins of intermittency. They found that this system was able to reproduce key features of inertial-range intermittency, such as heavy tails in the probability distribution of transverse velocity increments and negative skewness of the longitudinal velocity increments, starting from initial Gaussian conditions. Hamlington, Schumacher & Dahm (2008) and Leung, Swaminathan & Davidson (2012) examined vortical structures at different

scales and showed that their shape becomes more worm-like with decreasing scale and that they align with the most stretching direction of strain at scales several times larger than the vortical structures. In laboratory experiments, Sinhuber, Bewley & Bodenschatz (2017) found that oscillations in power-law behaviour for moments of longitudinal velocity increments occur at fixed multiples of the Kolmogorov length scale, independent of Reynolds number, revealing the influence of dissipation-range fluid motions on inertial-range velocity statistics. Danish & Meneveau (2018) used coarse-grained velocity fields in turbulence and investigated the population fractions of different flow topologies as a function of scale and connected them to alignment of coarse-grained vorticity.

We aim to add to this knowledge of inertial-range dynamics by investigating rods that naturally respond to features in the flow and become aligned by fluid motions whose scale is near the rod length. We also build on the previous results from laboratory experiments which investigated the rod tumbling rate (rate of change of rod orientation (Parsa & Voth 2014)) and the rod stretching rate (longitudinal velocity increment across the rod (Kramel *et al.* 2016)) for rods with lengths in the inertial range. To do so, we use direct numerical simulation (DNS) data of isotropic turbulence in which we compute the motion of long rods (or, equivalently, rigid material lines). Along rod trajectories, we record the fluid velocity gradients filtered at the scale of the particle. We explore how the rods align with these perceived velocity gradients; this alignment is important in explaining the dynamics of rod rotation and rod stretching rates as a function of rod length. Because the moments of rod rotation and rod stretching directly probe the degree of alignment and how it behaves for rare events, we check whether the refined similarity hypothesis is able correctly to predict these moments.

The remainder of this paper is organised as follows. In §2 we show the equations of rod motion and the methods used to track rods in a turbulent flow. This section also shows our method for computing the perceived velocity gradients around each rod as it travels through the flow. In §3, we discuss the results, starting with properties of the perceived velocity gradient tensor (§§3.1 and 3.2), and how these relate to the power-law behaviour of rod dynamics in the inertial range (§§3.3 and 3.4) and scaling exponents of their higher-order moments (§3.5). We end with the conclusions in §4.

2. Methods

2.1. *Equations of rod motion*

Figure 1(*a*) shows a planar slice of a turbulent fluid velocity field and a rigid, neutrally buoyant rod of length l and infinitesimal diameter suspended in it. Shin & Koch (2005) derived the equations of motion for a rod such as this in a turbulent velocity field from slender-body theory (Batchelor 1970; Cox 1970). Slender-body theory uses matched asymptotic expansions in which the particle is replaced by a line of forces. In the limit $\ln(2l/d_r) \gg 1$, where d_r is the rod diameter and (l/d_r) is the rod aspect ratio, Shin & Koch (2005) showed that the solution from slender-body theory could be simplified. To the same order of accuracy, they also showed that rod motion could be computed using one-way forcing, i.e. the reaction of the rod onto the fluid could be ignored. This is equivalent to ignoring the inertia of the rod in comparison to the inertia of the fluid at scale l. For our purposes, the rod can be considered to be of very small diameter (or very high aspect ratio) so that this approximation is valid. Under this approximation, we do not account for the influence of rods on the fluid velocity. We also do not account for the interactions between rods since we are
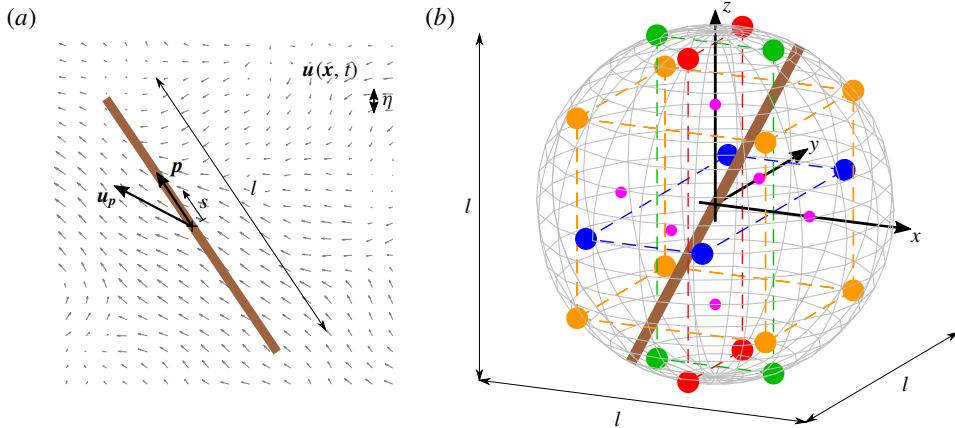
FIGURE 1. (Colour online) (*a*) A rigid, neutrally buoyant rod of length *l* with orientation vector p and with velocity of translation u_p suspended in a fluid velocity field $u(x, t)$. (*b*) Locations of velocity samples used to calculate the perceived velocity gradients around the rod. Large dots are on the surface of a sphere of diameter *l* and are the 20 vertices of a regular dodecahedron. Small dots within the sphere are the six vertices of a regular octahedron.

interested in the motion of an ensemble of rods rather than how rods affect each other. In this framework, the equations of motion for rod translation and rod orientation are, respectively,

$$u_p = \frac{1}{l} \int_{-l/2}^{l/2} u \, ds, \tag{2.1a}$$

$$\dot{p} = \frac{12}{l^3} \int_{-l/2}^{l/2} s[u - p(u \cdot p)] \, ds. \tag{2.1b}$$

The variables in (2.1) are defined in figure 1(*a*): u is the fluid velocity field, u_p is the rod translational velocity (velocity of the rod centre), p is a unit vector that indicates the rod orientation, $\dot{p}$ gives the rod rotation rate (we refer to this as the tumbling rate), and *s* is a dummy variable that measures distance along the rod from the rod centre.

Equation (2.1*a*) states that the rod translation velocity is the average of the fluid velocity sampled by the rod along its length. Equation (2.1*b*) states that the rod tumbling is given by integrating the moment about the rod centre of the fluid velocity component that is perpendicular to the rod orientation. In the limit $l \to 0$, the rod translational velocity equals the local fluid velocity and the rod acts as a fluid tracer. This simplifies (2.1*a*) to $u_p = u$. In this limit, equation (2.1*b*) can also be simplified since velocity variations are linear across the rod length. Also, u in (2.1*b*) can be replaced by $u - u_p$ without changing the equation. Thus, the quantity in square brackets in (2.1*b*) can be expressed in terms of the local velocity gradients. The correct expression, which considers the along-rod gradient of the velocity perpendicular to the rod, is given by $[Ap - (p \cdot Sp)p]s$, where A is the velocity gradient tensor and S is its symmetric part. Since the velocity gradients are uniform, they can be taken outside the integral, leaving (2.1*b*) to simplify to Jeffery's (1922) equation for tumbling of an infinite-aspect-ratio prolate spheroid:

$$\dot{p} = Ap - (p \cdot Sp)p. \tag{2.2}$$

The first term in this equation is responsible for rod tumbling whereas the second term serves to keep p to unit length.

In the limit $l \to 0$, the rod stretching rate is given by the along-rod gradient of the fluid velocity parallel to the rod, which is given by the expression $p \cdot Sp$. For longer rods, the stretching rate is given by the integral of $p \cdot Sp$ over the rod length divided by the rod length. The integral of $p \cdot Sp$ over the rod length simplifies to the longitudinal velocity increment between the rod end points,

$$\int_{-l/2}^{l/2} p^{\mathrm{T}} S p \, \mathrm{d}s = \Delta_r u, \qquad (2.3)$$

where $\Delta_r u$ denotes the fluid velocity increment across the rod length for the velocity component parallel to the rod.

In this paper, the rod dynamics we focus on are the rod tumbling rate, $\dot{p}$, and the rod stretching rate, $\Delta_r u/l$.

2.2. *Numerical computations*

We examine the dynamics of rods of different lengths in homogeneous isotropic turbulence. The turbulent fluid velocity field is taken from DNS data in the Johns Hopkins Turbulence Database (Perlman *et al.* 2007; Li *et al.* 2008; Yu *et al.* 2012). The forced isotropic turbulence dataset consists of velocity and pressure data on a triply periodic cubic domain where the Taylor-scale Reynolds number is $Re_\lambda \approx 430$. The ratio of the integral length scale, L, to the Kolmogorov length scale, η, is $L \approx 480\eta$, and the ratio of the integral time scale, T_L, to the Kolmogorov time scale, τ_η, is $T_L \approx 45\tau_\eta$.

Rods of length l spanning the range $\eta \leqslant l \leqslant 200\eta$ ($0.002L \leqslant l \leqslant 0.42L$) are tracked in the flow. The position and orientation of each rod are tracked by integrating discretised forms of (2.1) in which the rod is represented by a nine-point stencil. In sensitivity tests, it was found that using more than nine points to represent the rod gave only marginally improved accuracy for the variance of rod tumbling (less than 2.5 % even for the longest rods considered). The integrations are carried out using second-order Runge–Kutta algorithms with a time step of $0.009\tau_\eta$, which is twice the value of the time step used in the DNS integration. Rod data are recorded every five integration steps.

For each rod length, 7500 rods are initialised at random positions and random orientations and tracked from $t = 0$ to $t = 2T_L$. Initial-time statistics show the behaviour of randomly oriented rods and are calculated as an ensemble average over all rods at $t = 0$. Long-time statistics show the behaviour of rods in a statistically steady alignment with the turbulent flow and are calculated as an ensemble average over all rods and over time for $40\tau_\eta \leqslant t \leqslant 2T_L$. Rods of all lengths have reached a statistically steady alignment with the flow by $t = 40\tau_\eta$. Rod alignment is discussed in more detail in the following section.

2.3. *Perceived velocity gradient tensor*

In addition to tracking rod position and orientation, we also compute velocity gradients around each rod as it travels through the flow. For rods in the tracer limit, the relevant velocity gradients are given by the velocity gradient tensor along Lagrangian fluid trajectories, denoted as A. For longer rods, the relevant velocity

gradients are given by the 'perceived velocity gradient tensor', $\tilde{\boldsymbol{A}}$, along the rod trajectory. The tensor $\tilde{\boldsymbol{A}}$ shows gradients in fluid motion at the rod length scale, l.

We compute $\tilde{\boldsymbol{A}}$ by a least-squares fit to velocity data at sample points within a region of interest surrounding the rod following Chertkov *et al.* (1999) and Pumir *et al.* (2013). To do this, we use velocity data at 26 points distributed around the rod centre (figure 1*b*), where 20 points form a regular dodecahedron that can be circumscribed by a sphere of diameter l. The remaining six points form a regular octahedron whose vertices are at the centres of the six faces of the cube formed by eight vertices of the dodecahedron (orange circles in figure 1*b*). The orientation of both polyhedra with respect to the simulation grid is held constant, i.e. it does not depend on rod orientation. The distribution of these 26 points is chosen because it is isotropic and most of the data (20 points) are at a distance $l/2$ from the rod centre. Additionally, tests with fewer points arranged at the vertices of fewer-sided regular polyhedra showed that the rod tumbling variance calculated using the perceived velocity gradients and Jeffery's equation converged to within 2.5 % after using more points than the 20 vertices of the dodecahedron. To calculate the perceived velocity gradients, the fluid velocity at the rod centre is subtracted from the velocity at the 26 sample points. Then, $\tilde{\boldsymbol{A}}$ is computed from a least-squares fit (equation (4) in Pumir *et al.* 2013). Finally, continuity is imposed by subtracting $(1/3)\tilde{A}_{ii}\delta_{ij}$ from the least-squares solution to make the final $\tilde{\boldsymbol{A}}$ trace-free.

Like the velocity gradient tensor, the perceived velocity gradient tensor can be decomposed into a vorticity vector and a strain-rate tensor. Thus, there are four key directions associated with $\tilde{\boldsymbol{A}}$: the direction of vorticity, represented by the unit vector $\tilde{\boldsymbol{e}}_{\boldsymbol{\omega}}$, and the eigenvectors of the strain-rate tensor, represented by the unit vectors $\tilde{\boldsymbol{e}}_1$, $\tilde{\boldsymbol{e}}_2$, $\tilde{\boldsymbol{e}}_3$. The most extensional direction is labelled $\tilde{\boldsymbol{e}}_1$ and corresponds to the most positive eigenvalue, $\tilde{\lambda}_1$. The most compressional direction is labelled $\tilde{\boldsymbol{e}}_3$ and corresponds to the most negative eigenvalue, $\tilde{\lambda}_3$. The intermediate direction is $\tilde{\boldsymbol{e}}_2$ and corresponds to $\tilde{\lambda}_2$, which can take either sign. Continuity requires that $\tilde{\lambda}_1 + \tilde{\lambda}_2 + \tilde{\lambda}_3 = 0$. Within the constraints of continuity and the ordering of the eigenvalues, the strain state can be quantified with a single dimensionless number given by (Lund & Rogers 1994)

$$\tilde{s}^* = \frac{-3\sqrt{6}\,\tilde{\lambda}_1\tilde{\lambda}_2\tilde{\lambda}_3}{(\tilde{\lambda}_1{}^2 + \tilde{\lambda}_2{}^2 + \tilde{\lambda}_3{}^2)^{3/2}}. \tag{2.4}$$

Here $\tilde{s}^*$ varies in the range $[-1, +1]$; $\tilde{s}^* = +1$ is the limit of axisymmetric extension, where a spherical fluid element evolves into a disc, and $\tilde{s}^* = -1$ is the limit of axisymmetric contraction, where a spherical fluid element evolves into rod. The ratio $\tilde{\lambda}_2/\tilde{\lambda}_1$, which varies in the range $[-0.5, +1]$, is also helpful in picturing the strain state, with $\tilde{\lambda}_2/\tilde{\lambda}_1 = -0.5$ being the limit of axisymmetric contraction, and $\tilde{\lambda}_2/\tilde{\lambda}_1 = +1$ being the limit of axisymmetric extension. It is worth noting that the probability density function (p.d.f.) of $\tilde{\lambda}_2/\tilde{\lambda}_1$ at the extreme values vanishes due to kinematic reasons rather than a lack of existence of such strain states (see Lund & Rogers 1994).

2.4. *Lagrangian stretching directions*

The time evolution of rod orientation relative to the directions of the velocity gradient tensor is more intuitive in the Lagrangian framework given by the Cauchy–Green strain tensors than with respect to the instantaneous velocity gradients given by $\tilde{\boldsymbol{A}}$. For a fluid element undergoing deformation due to velocity gradients given by

$\tilde{\boldsymbol{A}}(t)$, the deformation gradient tensor, $\tilde{\boldsymbol{F}}$, is given by integrating the differential relation $\mathrm{d}\tilde{\boldsymbol{F}}(t)/\mathrm{d}t = \tilde{F}_{ij}(t)\tilde{A}_{jk}(t)$. We calculate $\tilde{\boldsymbol{F}}$ by carrying out this integration using a fourth-order Runge–Kutta algorithm with the initial condition $\tilde{\boldsymbol{F}}(t = 40\eta) = \delta_{ij}$. The integration is carried out for $40\eta \leqslant t \leqslant 2T_L$ during which rods are in a statistically steady alignment with the flow.

The deformation gradient tensor can be written as $\tilde{\boldsymbol{F}} = \tilde{\boldsymbol{R}}\tilde{\boldsymbol{U}}$ or as $\tilde{\boldsymbol{F}} = \tilde{\boldsymbol{V}}\tilde{\boldsymbol{R}}$, depending upon whether the deformation is described as stretching ($\tilde{\boldsymbol{U}}$) followed by rotation ($\tilde{\boldsymbol{R}}$) or rotation ($\tilde{\boldsymbol{R}}$) followed by stretching ($\tilde{\boldsymbol{V}}$) (see e.g. Gonzalez & Stuart 2009). Thus, $\tilde{\boldsymbol{U}}$ and $\tilde{\boldsymbol{V}}$ are the right and left stretch tensors, respectively. Using the inner product of $\tilde{\boldsymbol{F}}$ with itself, we can isolate the stretching components of the deformation gradient: $\tilde{\boldsymbol{C}}_R = \tilde{\boldsymbol{F}}^\mathrm{T}\tilde{\boldsymbol{F}} = \tilde{\boldsymbol{U}}^2$ or $\tilde{\boldsymbol{C}}_L = \tilde{\boldsymbol{F}}\tilde{\boldsymbol{F}}^\mathrm{T} = \tilde{\boldsymbol{V}}^2$, where $\tilde{\boldsymbol{C}}_R$ and $\tilde{\boldsymbol{C}}_L$ are the right Cauchy–Green strain tensor and the left Cauchy–Green strain tensor, respectively. The eigenframes of $\tilde{\boldsymbol{C}}_R$ and $\tilde{\boldsymbol{C}}_L$ provide useful descriptions of fluid strain and we denote the unit vectors in the most extensional directions (associated with the most positive eigenvalues) of these tensors as $\tilde{\boldsymbol{e}}_{R1}$ and $\tilde{\boldsymbol{e}}_{L1}$, respectively. Physically, $\tilde{\boldsymbol{e}}_{R1}$ is the direction of greatest fluid stretching at the initial time being considered and $\tilde{\boldsymbol{e}}_{L1}$ is the direction of greatest fluid stretching after taking into account the cumulative effect of velocity gradients over Δt.

2.5. *Scale-local time scales*

The characteristic time scale for fluid motions at rod length scale l is a 'scale-local' time scale. Two such time scales are constructed using two-point fluid velocity statistics, otherwise known as structure functions (see e.g. Pope 2000). If longitudinal velocity increments in the flow are denoted as $\Delta_L u$, and transverse velocity increments are denoted as $\Delta_N u$, $\langle(\Delta_L u)^2\rangle$ and $\langle(\Delta_N u)^2\rangle$ are the second-order longitudinal and transverse velocity structure functions, respectively. The scale-local time scales are then given by $\tau_L = l/(\sqrt{15\langle(\Delta_L u)^2\rangle})$ and $\tau_N = l/(\sqrt{(15/2)\langle(\Delta_N u)^2\rangle})$, respectively, where $\Delta_L u$ and $\Delta_N u$ are evaluated at scale l. Defined in this way, τ_L and τ_N transition smoothly from a value of τ_η in the limit of $l \to 0$ to a Kolmogorov (1941, henceforth K41) scaling in the inertial range, where τ_L and τ_N scale as $l^{2/3}$.

We compute τ_L and τ_N from $\Delta_L u$ and $\Delta_N u$ taken from velocity data at the 20 vertices of the dodecahedron used to compute $\tilde{\boldsymbol{A}}$. These form 10 pairs of points, where each pair consists of diametrically opposite points separated by distance l.

2.6. *Rod dynamics from Jeffery's equation and rod tumbling from rod end points*

We will refer to rod dynamics, i.e. position, orientation, velocity and tumbling, obtained by integrating (2.1) as 'fully resolved' rod dynamics. These data will be compared to rod dynamics obtained from two alternative methods, which we now introduce.

The first alternative method is to compute rod orientation and tumbling via integration of Jeffery's equation using the perceived velocity gradient tensor, $\tilde{\boldsymbol{A}}(t)$, along each rod trajectory. This is done by integrating equation (2.2) using a fourth-order Runge–Kutta algorithm with the same initial conditions as the fully resolved rod dynamics. Rod orientation and tumbling obtained using Jeffery's equation are denoted as $p_{i,J}$ and $\dot{p}_{i,J}$, respectively.

The second alternative method pertains only to the rod tumbling. In this method, the rod trajectories and the rod orientation time histories from fully resolved rod dynamics are used, but an alternative measure of rod tumbling is computed using only the fluid velocity at the rod end points. If only the rod end points are used, (2.1b) simplifies to
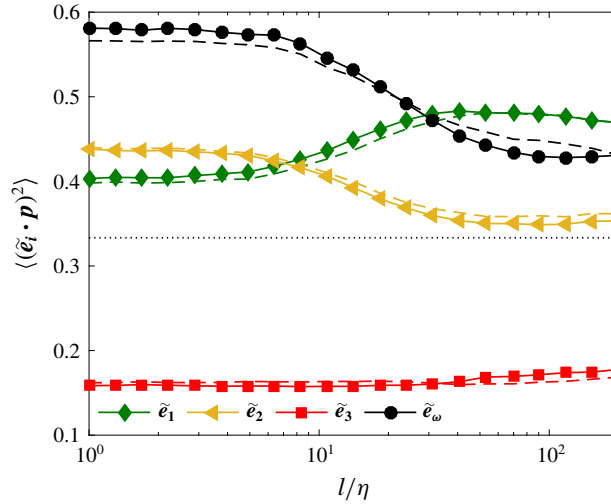
FIGURE 2. (Colour online) Mean rod alignment with the directions of $\tilde{\boldsymbol{A}}$ as a function of l/η. Symbols are data from fully resolved rod dynamics and dashed lines are data from integrating Jeffery's equation. The dotted line is at a value of $1/3$, which corresponds to random alignment.

$\Delta_r[\boldsymbol{u} - \boldsymbol{p}(\boldsymbol{u} \cdot \boldsymbol{p})]/l$, where $\Delta_r[\boldsymbol{u} - \boldsymbol{p}(\boldsymbol{u} \cdot \boldsymbol{p})]$ is the transverse velocity increment across the rod. In other words, the rod tumbling is determined by the increment of the fluid velocity across the rod length using the component perpendicular to the rod. The rod tumbling obtained in this way is denoted as $\dot{p}_{i,E}$.

3. Results

3.1. *Rod alignment*

Figure 2 shows the rod alignment for fully resolved rod dynamics and rod dynamics from integrating Jeffery's equation. Rod alignment is quantified by the inner product between the rod orientation $\boldsymbol{p}$ and the directions associated with $\tilde{\boldsymbol{A}}$. Mean-square values close to 1 indicate a propensity for the two vectors to be aligned with each other and mean-square values close to 0 indicate a propensity for the two vectors to be orthogonal to each other. Two unit vectors with no correlation in their alignment would produce a mean-square value of $1/3$. The data show that there is a scale-independent preferred alignment of rods in the tracer limit ($l < 5\eta$) that follows the order $\tilde{\boldsymbol{e}}_\omega > \tilde{\boldsymbol{e}}_2 > \tilde{\boldsymbol{e}}_1$ (see also Pumir & Wilkinson 2011; Chevillard & Meneveau 2013; Byron *et al.* 2015; Ni *et al.* 2015; Pujara & Variano 2017). As the rod length transitions to the inertial range, rod alignment with $\tilde{\boldsymbol{e}}_\omega$ decreases and rod alignment in the strain-rate eigenframe shifts from being more aligned with $\tilde{\boldsymbol{e}}_2$ to being more aligned with $\tilde{\boldsymbol{e}}_1$. There appears to be an almost scale-independent preferred rod alignment in the inertial range ($l > 60\eta$) that follows the order $\tilde{\boldsymbol{e}}_1 > \tilde{\boldsymbol{e}}_\omega > \tilde{\boldsymbol{e}}_2$.

The agreement in figure 2 between data from fully resolved rod dynamics and data from integrating Jeffery's equation using $\tilde{\boldsymbol{A}}$ shows that $\tilde{\boldsymbol{A}}$ captures the flow features that are responsible for rod tumbling. This is not surprising given that velocity increments separated by length l have the greatest weight in determining the rod tumbling rate in (2.1*b*) and also in computing $\tilde{\boldsymbol{A}}$. The p.d.f.s of alignment (not plotted) show that alignment in fully resolved rod dynamics tends to be slightly more skewed than in
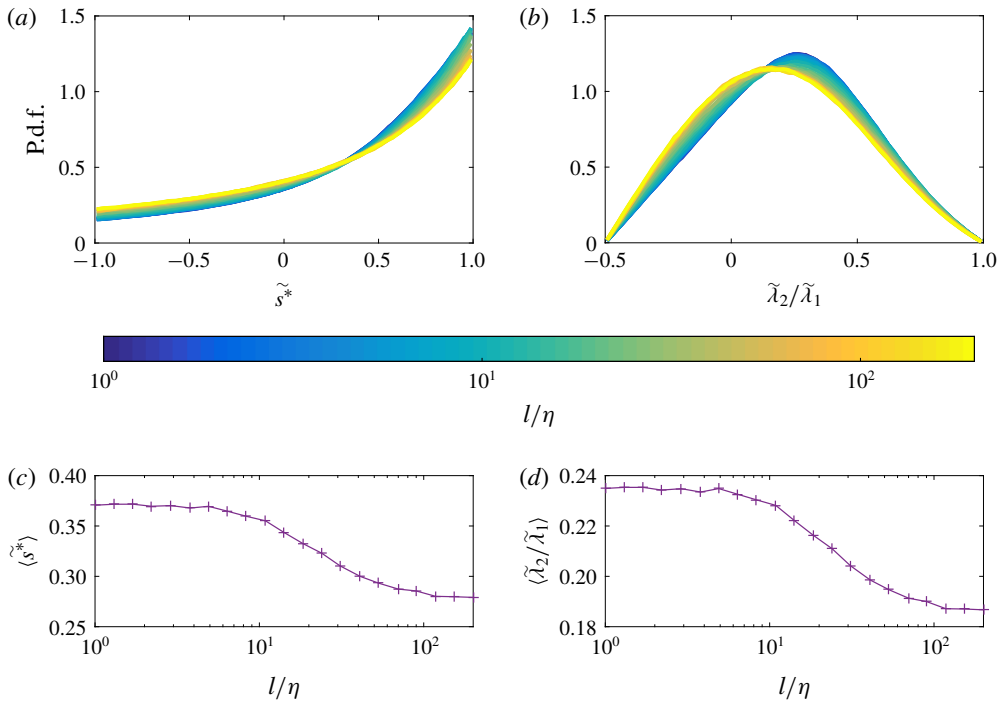
FIGURE 3. (Colour online) Properties of $\tilde{\mathbf{S}}$ as a function of l/η: (*a*) p.d.f.s of the strain state, $\tilde{s}^*$; (*b*) p.d.f.s of the ratio of eigenvalues $\tilde{\lambda}_2/\tilde{\lambda}_1$; (*c*) mean value of $\tilde{s}^*$; and (*d*) mean value of $\tilde{\lambda}_2/\tilde{\lambda}_1$.

rod data obtained from Jeffery's equation, but the net effect of this difference on the mean alignment value is small, as seen in figure 2. Having checked that $\tilde{\mathbf{A}}$ is able to reproduce the statistics of rod orientation, we can proceed to understand rod alignment in terms of the properties of $\tilde{\mathbf{A}}$.

Figure 3 shows how the properties of the perceived strain-rate tensor, and in particular the strain state, change with scale. At the smallest scale ($l = \eta$), the data are similar to those in Lund & Rogers (1994). The most likely strain state for all scales is $\tilde{s}^* = +1$ (axisymmetric extension), but the likelihood of $\tilde{s}^* = -1$ (axisymmetric contraction) increases with increasing scale. This changing distribution of the strain state provides at least a partial explanation for changing rod alignment with $\tilde{e}_1$: with increasing l/η, strain states tend towards one dominant direction of stretching, which improves rod alignment with this direction. In other words, there is less competition for rod alignment between $\tilde{e}_1$ and $\tilde{e}_2$ allowing rods to be more aligned with $\tilde{e}_1$.

The effects of a time delay on rod alignment are shown in figure 4. Figure 4(*a*) shows that rods have a maximum in alignment with $\tilde{e}_{R1}$ for some positive value of Δt. For longer rods, the maximum value is higher and occurs at smaller multiples of the scale-local time scale τ_N. The maxima in figure 4(*a*) indicate that, for a strain-rate tensor $\tilde{\mathbf{S}}$ at a given time t_0, the strongest alignment of rods with the most stretching direction of $\tilde{\mathbf{S}}(t_0)$ occurs with some optimum time delay at $t_0 + \Delta t$. When rod alignment is computed with respect to $\tilde{e}_{L1}$, figure 4(*b*) shows that it reaches a steady-state plateau. For longer rods, the plateaued alignment is weaker, but it is
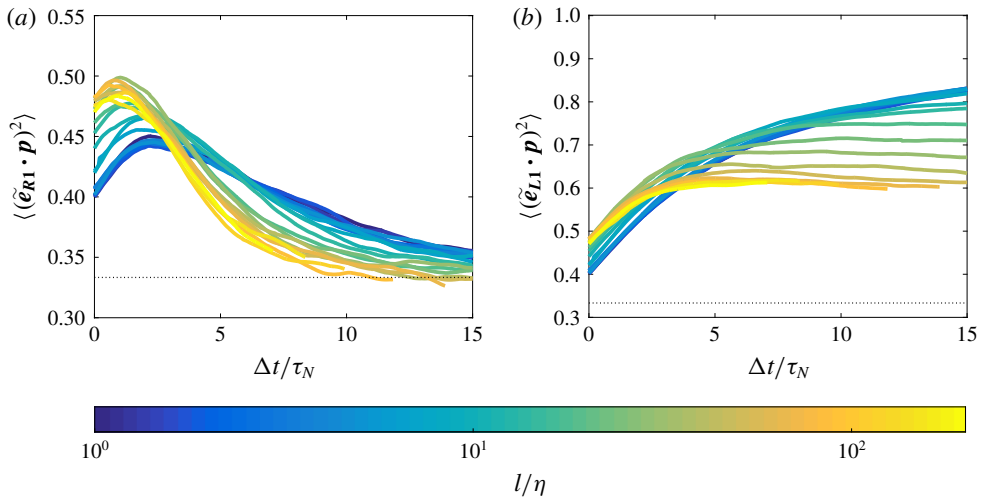
FIGURE 4. (Colour online) Alignment of rods with the most stretching direction of the right and left Cauchy–Green strain tensors as a function of the time delay. (*a*) Mean alignment between rods and $\tilde{e}_{R1}$. (*b*) Mean alignment between rods and $\tilde{e}_{L1}$. The dotted lines are at a value of $1/3$, which corresponds to random alignment.

reached in smaller multiples of τ_N. Rod alignment with $\tilde{e}_{L1}$ shows the rod response to the cumulative effects of the strain-rate tensor over a time Δt. Ni *et al.* (2014) showed that tracer rods approach perfect alignment with e_{L1} given a large enough Δt, consistent with the fact that rod orientation in the tracer limit is driven only by the term Ap (2.2). In contrast, figure 4(*b*) shows that rods outside of the tracer limit do not reach perfect alignment with $\tilde{e}_{L1}$. With increasing rod length, the decreasing plateau of alignment with $\tilde{e}_{L1}$ indicates that fluid motions at scales smaller than l prevent perfect rod alignment with $\tilde{e}_{L1}$. This is confirmed by the alignment of e_{L1} with p_J, where rod orientations are obtained from integrating Jeffery's equation and fluid motions at scales smaller than l are removed in $\tilde{A}$ from coarse-graining. In this case, we find that plots of $\langle (\tilde{e}_{L1} \cdot p_J)^2 \rangle$ against $\Delta t/\tau_N$ (not shown) collapse for rods of all lengths and show an approach towards perfect alignment.

In figures 2 and 4, the statistics of rod alignment are weakly non-monotonic with increasing l/η. In figure 2 the mean rod alignment with $\tilde{e}_1$ becomes stronger in the inertial range with a 'bump' at $l \approx 60\eta$. Figure 4(*a*) shows a similar variation in the maximum rod alignment with $\tilde{e}_{R1}$ as a function of l/η. The monotonic variation in the properties of $\tilde{S}$ in figure 3 show that this 'bump' cannot be explained by the p.d.f. of $\tilde{s}^*$. More likely, it is caused by the changing structure of time correlations for the elements of $\tilde{A}$ as a function of l/η.

3.2. *Vorticity alignment*

The alignment of vorticity in the strain-rate eigenframe of $\tilde{S}$ is an important property of $\tilde{A}$ for turbulent flow. Figure 5 shows how this alignment changes with l/η using the same statistical measures as in the previous section. In figure 5(*a*), we see that the alignment between $\tilde{e}_\omega$ and $\tilde{e}_1$ increases with increasing scale, whereas the alignment between $\tilde{e}_\omega$ and $\tilde{e}_2$ decreases with increasing scale. The orthogonality between $\tilde{e}_\omega$ and $\tilde{e}_3$ also decreases with increasing scale. These results are consistent with previous
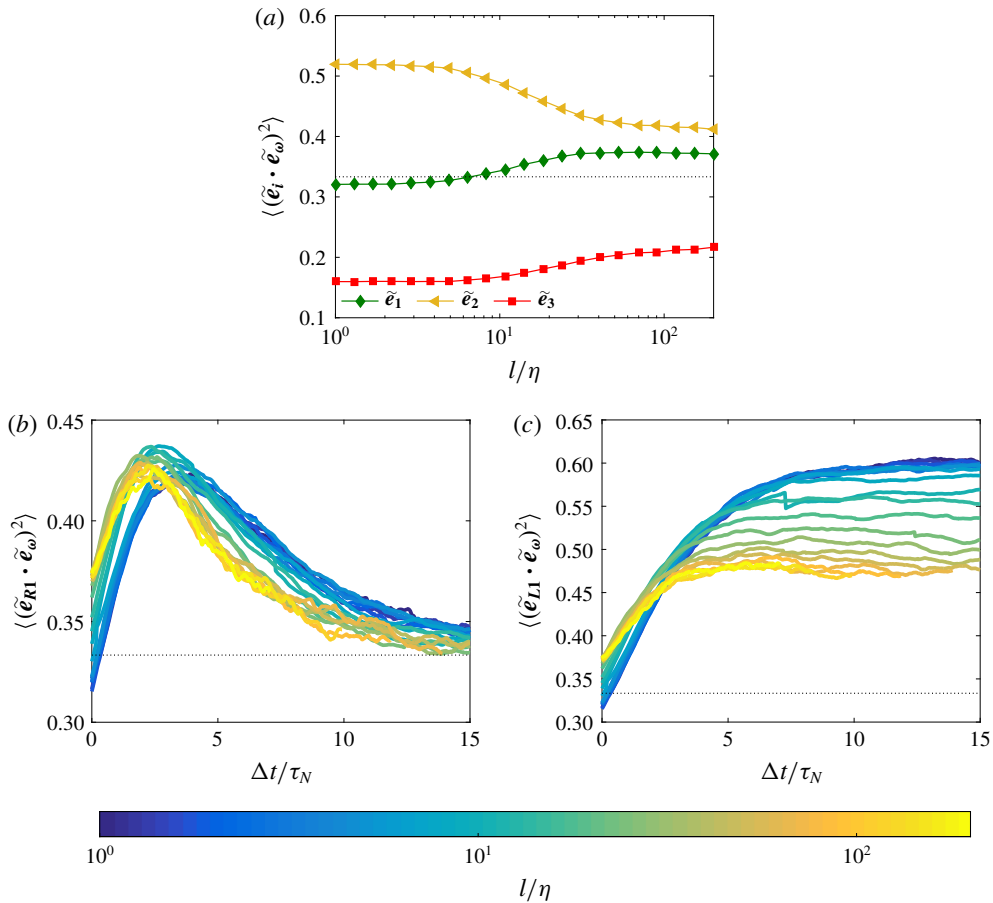
FIGURE 5. (Colour online) Alignment of vorticity in the strain-rate and Cauchy–Green eigenframes as a function of scale. (*a*) Mean alignment of $\tilde{\boldsymbol{e}}_{\omega}$ within the perceived strain-rate eigenframe. (*b*) Mean alignment between the $\tilde{\boldsymbol{e}}_{\omega}$ and $\tilde{\boldsymbol{e}}_{R1}$. (*c*) Mean alignment between the $\tilde{\boldsymbol{e}}_{\omega}$ and $\tilde{\boldsymbol{e}}_{L1}$. The dotted lines are at a value of $1/3$, which corresponds to random alignment.

data (Luthi *et al.* 2007; Pumir *et al.* 2013; Danish & Meneveau 2018) where $\tilde{\boldsymbol{A}}$ was computed using different coarse-graining methods. In figure 5(*b*), we see that vorticity reaches a peak alignment with $\boldsymbol{e}_{R1}$ after a time delay of $\Delta t \approx 3\tau_N$, almost independent of the scale l/η (Xu *et al.* 2011; Pumir *et al.* 2013). The initial growth in alignment of vorticity with $\boldsymbol{e}_{R1}$ is consistent with previous arguments for the evolution of vorticity in the tracer limit, i.e. it is caused by the vortex stretching term in the dynamical equation of $\boldsymbol{A}$ (Chevillard & Meneveau 2011; Ni *et al.* 2015). Outside the tracer limit, the curves are nearly scale-independent when time is made dimensionless by the scale-local time scale, τ_N. This shows that small-scale motions do not affect the alignment of coarse-grained vorticity with $\boldsymbol{e}_{R1}$. In figure 5(*c*), we see that vorticity alignment with $\boldsymbol{e}_{L1}$ increases with time until it reaches a plateau. The plateau's value decreases with increasing scale, which shows that smaller scales disrupt the alignment of vorticity with the direction of greatest stretching given by the cumulative deformation of the strain-rate tensor.

The above results point towards a partial analogy between infinitesimal rods and vorticity in turbulent flows. As pointed out previously (Pumir & Wilkinson 2011), the vortex stretching term, $\boldsymbol{S}\boldsymbol{\omega}$, in the vorticity evolution equation has an analogous term in Jeffery's equation for evolution of rod orientation, $\boldsymbol{S}\boldsymbol{p}$. However, unlike rods, vorticity is an active vector that is coupled to the strain rate in its evolution equation and affected by viscosity (e.g. Guala *et al.* 2005; Luthi, Tsinober & Kinzelbach 2005; Pumir & Wilkinson 2011). Hence, unlike rods, vorticity does not reach perfect alignment with $\boldsymbol{e}_{L1}$ in the tracer limit. With increasing l/η, the action of fluid motions at scales smaller than l on dynamics at scale l leads to decreasing plateaus of alignment with $\boldsymbol{e}_{L1}$ for both rods and coarse-grained vorticity, but the effects of smaller scales on coarse-grained vorticity are more complex since the vorticity also affects the velocity field. This makes the dynamics of rods and vorticity diverge even further with increasing l/η, as indicated by the decreased alignment between rods and vorticity in figure 2.

3.3. *Lower-order moments of rod tumbling*

The rod tumbling rate is best characterised in terms of its variance, $\langle \dot{p}_i \dot{p}_i \rangle$, since the mean of any single component of the rod tumbling vector is zero due to flow isotropy. For randomly oriented rods, the rod tumbling variance can be derived from (2.1*b*) to be (see Olson & Kerekes 1998; Shin & Koch 2005):

$$\langle \dot{p}_i \dot{p}_i \rangle \tau_N^2 = \frac{16/5}{l[1 - R_{NN}(l)]} \int_0^l \left[1 - \frac{3s}{l} + \left(\frac{2s}{l} \right)^3 \right] R_{NN}(s) \, \mathrm{d}s, \quad (3.1)$$

where R_{NN} is the dimensionless transverse velocity correlation function.

In the tracer limit, equation (3.1) simplifies to $\langle \dot{p}_i \dot{p}_i \rangle \tau_N^2 = 4/15$ (Shin & Koch 2005) since the transverse velocity correlation can be written in terms of the velocity gradients, whose variance can in turn be written in terms of the mean dissipation rate in isotropic turbulence (Pope 2000). In the inertial range, K41 parametrisations can be used to simplify (3.1). From K41 theory, $R_{NN} = 1 - (2/3u_{rms}^2)C_2(\langle \epsilon \rangle l)^{2/3}$ and $\tau_N = (l^2/\langle \epsilon \rangle)^{1/3}/\sqrt{10C_2}$, where C_2 is a universal constant and is set to 2.0 here. From these expressions, equation (3.1) simplifies to $\langle \dot{p}_i \dot{p}_i \rangle \tau_N^2 = 108/350$ for rods in the inertial range. The inertial-range result can also be expressed in terms of the Kolmogorov scales as $\langle \dot{p}_i \dot{p}_i \rangle \tau_\eta^2 = (108/35)C_2(l/\eta)^{-4/3}$, revealing that rod tumbling variance for randomly oriented rods in the inertial range should scale as $\langle \dot{p}_i \dot{p}_i \rangle \sim l^{-4/3}$. Parsa & Voth (2014) derived this expression and also provided a physical argument: rod tumbling in the inertial range is driven primarily by turbulent motions of size l and thus the rod tumbling variance should scale as the inverse square of the turnover time of these turbulent motions.

Figure 6(*a*) shows that the initial-time data (randomly oriented rods) agree well with the prediction from K41 theory ($\langle \dot{p}_i \dot{p}_i \rangle \tau_\eta^2 = (108/35)C_2(l/\eta)^{-4/3}$) in the inertial range ($l > 60\eta$). These data are examined more closely in figure 6(*b*), where they are made dimensionless using the scale-local time scale τ_N. There is good agreement with the predictions in the tracer limit: $\langle \dot{p}_i \dot{p}_i \rangle \tau_N^2 = 4/15$ for $l < 5\eta$. In the transition to the inertial range, there is a non-monotonic variation (or 'bump') before the data show agreement with the inertial-range prediction: $\langle \dot{p}_i \dot{p}_i \rangle \tau_N^2 = 108/350$ for $l > 100\eta$. The non-monotonic variation between the tracer limit value and the inertial-range value shows that transverse velocity increments, which are used to compute τ_N, start to show inertial-range scaling at lower values of l/η compared to rod tumbling.
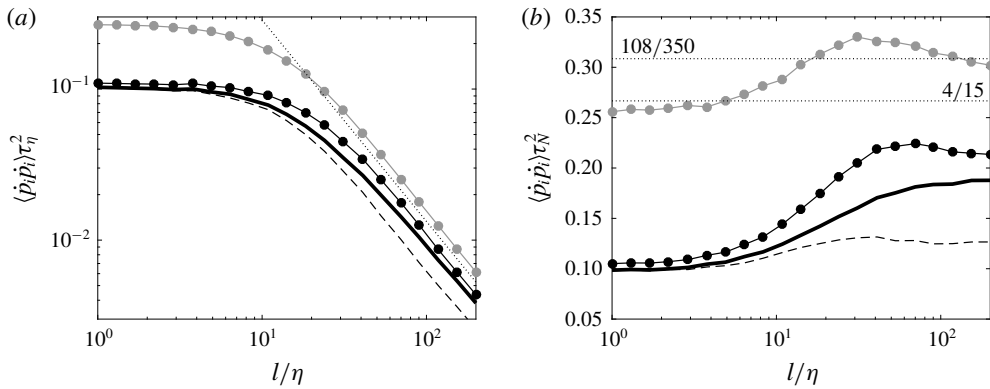
FIGURE 6. Variance of rod tumbling calculated from (i) fully resolved rod data, $\langle \dot{p}_i \dot{p}_i \rangle$ (circles), (ii) Jeffery's equation, $\langle \dot{p}_i \dot{p}_i \rangle_J$ (dashed line), and (iii) rod end points, $\langle \dot{p}_i \dot{p}_i \rangle_E$ (thick line). Initial-time data are shown in grey and long-time data in black. (a) Variance of rod tumbling made dimensionless by τ_η (dotted line is $(108/35)C_2(l/\eta)^{-4/3}$). (b) Variance of rod tumbling made dimensionless by τ_N.

Physically, this means that considering only the velocity increments across the rod length underpredicts the rod tumbling variance at transition scales for randomly oriented rods.

The long-time values of rod tumbling variance are significantly lower than the initial-time values because rods of all lengths show preferential alignment with the fluid vorticity, which suppresses their tumbling (Parsa *et al.* 2012). The behaviour of rod tumbling variance for rods in statistically steady equilibrium with the turbulent flow, i.e. the long-time data, shows a non-monotonic variation, similar to the initial-time data. Though its size and location are changed, the cause of the 'bump' in the long-time data is again the difference between transverse velocity increments and the transverse velocity correlation function, where both quantities are now evaluated in the frame of the rod. This is demonstrated by the fact that data from using only the rod end points ($\dot{p}_{i,E}$) show a monotonic increase from the dissipation range to the inertial range without a 'bump'.

The configuration of alignment in figure 2 is responsible for reducing the size of the 'bump', meaning that preferential rod alignment causes the value of $\langle \dot{p}_i \dot{p}_i \rangle \tau_N^2$ to be flatter in the inertial range and improves the agreement with the $\langle \dot{p}_i \dot{p}_i \rangle \sim l^{-4/3}$ scaling. Rod alignment is not accounted for in Parsa & Voth's (2014) physical argument that rod tumbling in the inertial range is driven primarily by turbulent motions of size l, but it appears that preferential rod alignment causes the rod tumbling variance to better agree with predictions made from this argument.

3.4. *Lower-order moments of rod stretching*

The p.d.f.s of rod stretching are shown in figure 7(a) with their moments shown in figure 7(b–e). In most cases, the rod stretching has been made dimensionless with the scale-local time scale τ_L. In this dimensionless form, the longitudinal velocity increments across the rod are normalised by longitudinal velocity increments in random orientations, thereby making the effects of rod alignment explicit.

The initial-time mean of rod stretching, $\langle \Delta_r u/l \rangle$, vanishes due to fluid incompressibility, but the long-time value of $\langle \Delta_r u/l \rangle$ is not zero because rods
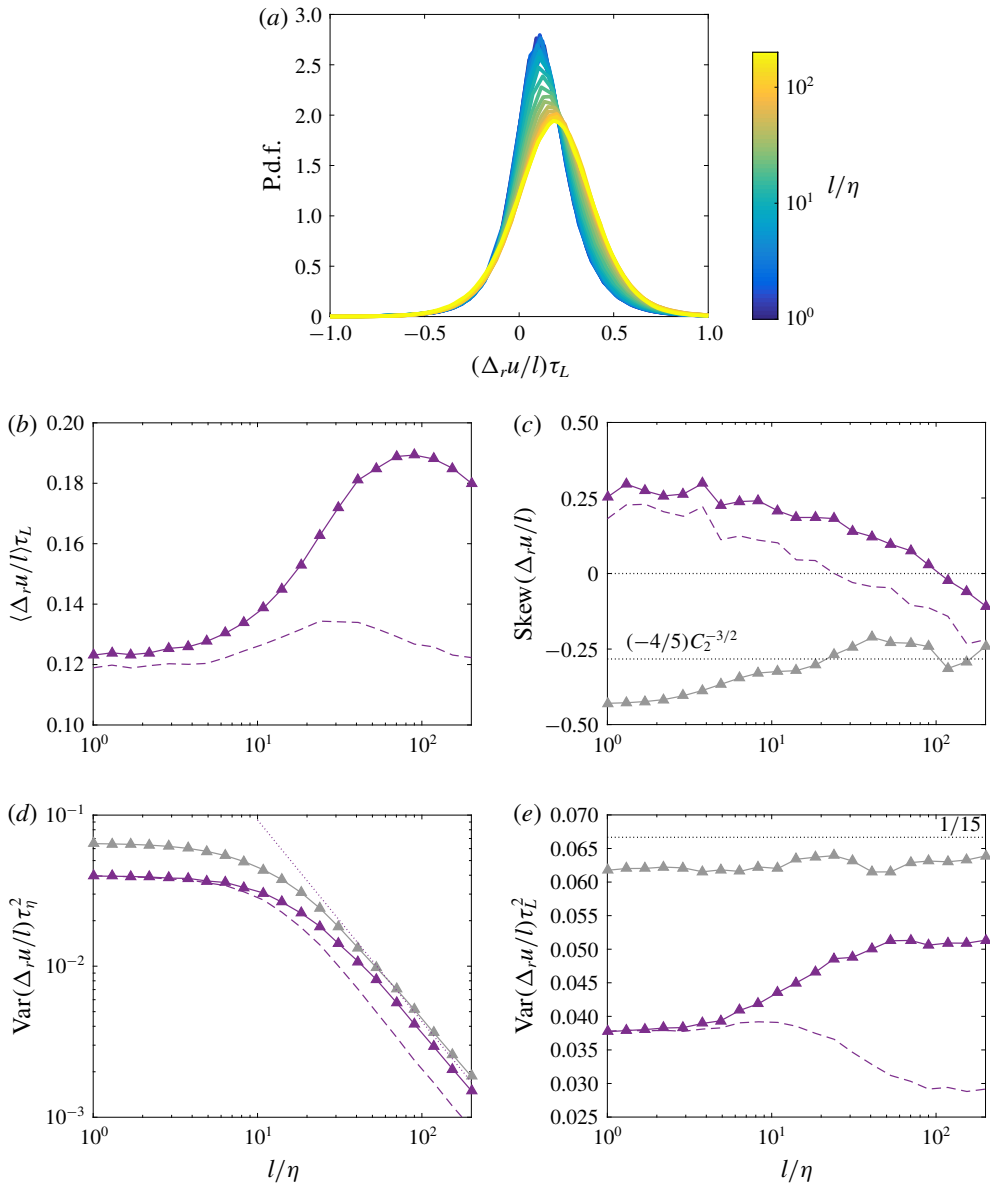
FIGURE 7. (Colour online) Statistics of rod stretching as a function of l/η: (i) from fully resolved rod data, $(\Delta_r u/l)$ (triangles), and (ii) from Jeffery's equation, $(\Delta_r u/l)_J$ (dashed lines). Initial-time data are shown in grey and long-time data in purple. (*a*) P.d.f.s of the long-time values of $(\Delta_r u/l)\tau_L$ from fully resolved rod data. (*b*) Mean value, $\langle\Delta_r u/l\rangle\tau_L$. (*c*) Skewness value, Skew$(\Delta_r u/l)$. (*d*) Variance value normalised by the Kolmogorov time scale, Var$(\Delta_r u/l)\tau_\eta^2$ with the dotted line showing $C_2(l/\eta)^{-4/3}$. (*e*) Variance value normalised by scale-local time scale, Var$(\Delta_r u/l)\tau_N^2$ with the dotted line as labelled.

show preferential alignment in the perceived strain-rate eigenframe. The effects of preferential rod alignment on the mean rod stretching can be observed in figure 7(*b*). It shows that $\langle\Delta_r u/l\rangle\tau_L$ increases non-monotonically from a value of approximately

0.12 in the tracer limit to a value of approximately 0.18 in the inertial range, with a small 'bump' at $l \approx 100\eta$. The tracer limit result is in agreement with previous data (Girimaji & Pope 1990). Given that rod stretching is achieved by strain at the scale of the rod length, it is not surprising that the non-monotonic variation in $\langle \Delta_r u/l \rangle \tau_L$ reflects the non-monotonic variation in alignment between $\boldsymbol{p}$ and $\tilde{\boldsymbol{e}}_1$ in figure 2. In particular, the location of the 'bump' in the mean rod stretching from Jeffery's equations, $\langle \Delta_r u/l \rangle_J \tau_L$, almost exactly matches the location of the 'bump' in $\langle (\tilde{\boldsymbol{e}}_1 \cdot \boldsymbol{p})^2 \rangle$.

Figure 7(c) shows the skewness of rod stretching, which is defined as $\text{Skew}(a) = \langle (a - \langle a \rangle)^3 \rangle / \langle (a - \langle a \rangle)^2 \rangle^{3/2}$. Since the mean stretching is zero for randomly oriented rods, the initial-time value of skewness is equivalent to the third-order longitudinal velocity structure function in the inertial range and to the third moment of longitudinal velocity gradients in the tracer limit. In this case, the data show agreement with Kolmogorov's 4/5th law in the inertial range, $\langle \Delta_r u^3 \rangle / \langle \Delta_r u^2 \rangle^{3/2} \approx -(4/5)C_2^{-3/2}$, and with previous data in the tracer limit $\langle \Delta_r u^3 \rangle / \langle \Delta_r u^2 \rangle^{3/2} \approx -0.4$ (summarised in Sreenivasan & Antonia (1997) and Davidson (2015)). The long-time rod stretching skewness data reflect the fact that rod alignment alters the rod stretching statistics. Alignment changes the sign of the rod stretching skewness so that the long-time value is positive for $l < 100\eta$. As l/η increases, the long-time skewness value decreases from $\text{Skew}(\Delta_r u/l) \approx 0.25$ for tracer rods (see also Kramel *et al.* 2016) and becomes negative after crossing zero at $l \approx 100\eta$. The negative values for rods well into the inertial range suggests that long rods experience stronger extremes of compression than of extension. It is also interesting to note that our data do not appear to show a scale-invariant behaviour for the long-time skewness for rods with lengths in the inertial range.

The variance of rod stretching, defined as $\text{Var}(a) = \langle (a - \langle a \rangle)^2 \rangle$, is shown in figure 7(d,e). Figure 7(d) shows that the variance of rod stretching follows a power-law scaling $\text{Var}(\Delta_r u/l) \sim l^{-4/3}$ in the inertial range. The physical argument behind this scaling is the same as that for the rod tumbling variance: rod stretching is driven primarily by fluid motions of size l, whose turnover time scales as $\sim l^{2/3}$ in the inertial range from K41 theory.

In figure 7(e), we plot the rod stretching variance made dimensionless by the scale-local time scale τ_L^2 to further examine the $l^{-4/3}$ scaling. At the initial time, rod stretching variance and τ_L^2 are essentially the same quantities with different constants and the initial-time variance of rod stretching rate can be written as $\text{Var}(\Delta_r u/l)\tau_L^2 = 1/15$. At long time, the value of $\text{Var}(\Delta_r u/l)\tau_L^2$ is lower than at the initial time because preferential alignment of rods means they sample a smaller variation of stretching and compression compared to randomly oriented rods. As l/η increases, rod alignment with the perceived velocity gradients weakens, causing $\text{Var}(\Delta_r u/l)\tau_L^2$ to increase towards the random orientation limit. Data of rod stretching variance from Jeffery's equation at long time show a decrease relative to τ_L^2 as l/η increases; this is due to the fact that velocity gradients in $\tilde{\boldsymbol{A}}$ are weaker than two-point velocity increments.

3.5. *Higher-order moments of rod tumbling and rod stretching*

The power-law behaviour of higher-order moments of rod tumbling and rod stretching can be used to understand how internal intermittency affects rod dynamics. One manifestation of intermittency in the inertial range is that power-law exponents of the moments of velocity increments, i.e. structure functions, show anomalous scaling

(Frisch 1995). From figures 6 and 7, we conclude that the variances of rod tumbling and rod stretching in the inertial range are primarily due to velocity increments over a distance l. This implies that intermittency corrections for higher-order moments of rod dynamics should behave similarly to those for velocity increments in the flow. To test this, we compare the power-law scaling exponents for moments of rod tumbling, $(\dot{p}_i\dot{p}_i)^{1/2}$, and rod stretching, $(\Delta_r u - \langle \Delta_r u \rangle)$, to those of transverse velocity increments, $\Delta_N u$, and longitudinal velocity increments, $\Delta_L u$. The moments of rod stretching are calculated after removing the mean, but results are unaffected within the statistical uncertainty because the mean is small compared to the standard deviation (figure 7*a*). To facilitate comparison to other quantities, rod tumbling is converted into velocity units by multiplying by the rod length, $(\dot{p}_i\dot{p}_i)^{1/2}l$. This does not affect the deviation of its power-law exponents from K41 predictions.

The power-law exponents are measured over $80\eta \leqslant l \leqslant 200\eta$. Over this range, logarithmic derivatives calculated using finite differencing are reasonably flat for all quantities, confirming power-law behaviour. It is known that the range of scales for which there is clear power-law behaviour is different for $\Delta_L u$ and $\Delta_N u$, as well as being a function of moment order and Reynolds number (Ishihara, Gotoh & Kaneda 2009), but for moments up to $n = 6$, $\Delta_L u$ and $\Delta_N u$ both show power-law behaviour over $80\eta \leqslant l \leqslant 200\eta$. In plots of pre-multiplied moments (not shown), we also observe reasonable convergence of moments up to $n = 6$ in our data. We compute the power-law scaling exponents by a least-squares fit in log space with error bars to show 95 % confidence intervals from the uncertainty in the fitting. Comparison of these results with scaling exponents calculated using extended self-similarity (not shown), where higher-order moments are plotted as a function of the second-moment instead of as a function of l, show that the results are the same within the statistical uncertainty.

The scaling exponents of higher-order moments are compared to predictions from the Kolmogorov hypotheses (K41 theory) and the refined Kolmogorov hypotheses (Kolmogorov 1962; Oboukhov 1962; henceforth K62 theory). In K41 theory, moments of velocity increments in the inertial range conditioned on the mean dissipation rate, $\langle \epsilon \rangle$, are assumed to be universal and to scale as $\langle (\Delta_L u)^n \rangle \sim (\langle \epsilon \rangle l)^{\zeta_n}$, where ζ_n is a function only of n and universal constants. The K41 prediction is $\zeta_{n,K41} = n/3$. However, it is well known that internal intermittency causes deviations from the K41 predictions (Frisch 1995; Sreenivasan & Antonia 1997). Taking the intermittent spatial distribution of dissipation into account, K62 theory predicts that $\zeta_{n,K62} = (n/3) - \mu(n/6)[(n/3) - 1]$. Here, μ is the intermittency exponent whose value is set to $\mu = 0.25$ (Pope 2000). This model of intermittency assumes that a locally averaged value of ϵ is sufficient to predict statistics of velocity increments and that the dissipation follows a log-normal distribution.

The scaling exponent data are shown in figure 8. In figure 8(*a*), we observe that $\Delta_N u$ shows a larger departure from K41 theory than $\Delta_L u$, which is in agreement with previous data (e.g. Chen *et al.* 1997), though data from higher-Reynolds-number simulations suggest that this difference exists only at low Reynolds numbers (Iyer, Sreenivasan & Yeung 2017). In figure 8(*b*), we include data of rod dynamics, first examining initial-time data of $\dot{p}_i$ (data where rods are randomly oriented). These scaling exponents match those of the transverse velocity increments quite well. Figure 8(*c*) shows data for rods in statistically steady alignment with the flow, computed from rod dynamics using velocity increments across the rod end points, $\dot{p}_{i,E}$ (rod tumbling computed using only rod end points) and $\Delta_r u - \langle \Delta_r u \rangle$ (rod stretching). Since these rod data are computed using two-point velocity increments aligned with
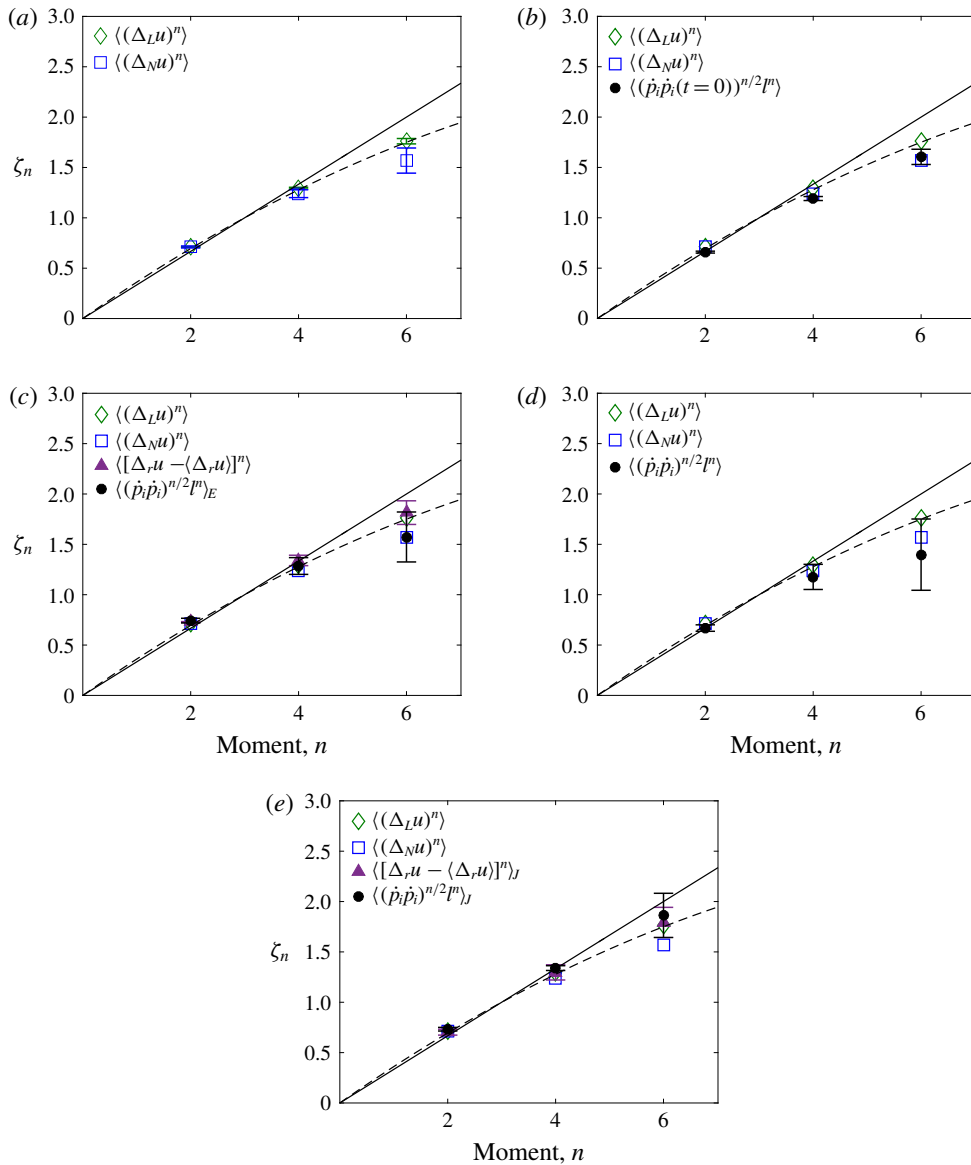
FIGURE 8. (Colour online) The power-law exponents for moments of velocity increments and rod dynamics in the inertial range as a function of moment order. K41 theory, $\zeta_n = n/3$ (solid line); K62 theory, $\zeta_n = (n/3) - \mu(n/6)[(n/3) - 1]$ with intermittency exponent $\mu = 0.25$ (dashed line). Error bars represent 95 % confidence intervals to the power-law fit.

the rod, they should explicitly reveal the effects of preferential alignment on scaling exponents. The scaling exponents of rod tumbling match the transverse velocity increments and those of rod stretching match the longitudinal velocity increments. Thus, it appears that rod alignment does not affect the intermittency within the statistical uncertainty in our data.

In figure 8(*d*), the rod tumbling data from using fully resolved rod dynamics for rods in statistically steady alignment with the flow are used to compute the scaling exponents. In this case, we observe that the scaling exponents of higher-order moments of rod tumbling show a further departure from K41 theory than transverse velocity increments. The statistical uncertainty associated with these data is large, but, within this uncertainty, it does seem that rod tumbling is more intermittent than transverse velocity increments in the flow. If this additional intermittency is real, it must be due to the distribution of transverse velocity over the rod length, which evidently increases the likelihood of extreme values of rod tumbling.

Finally, in figure 8(*e*), we show scaling exponents from rod data computed from Jeffery's equation. In this case, we observe that rod dynamics shows less intermittency compared to velocity increments in the flow. This shows that our computation of $\tilde{\boldsymbol{A}}$ not only gives weaker velocity gradients, but also leads to less intermittent rod dynamics, compared to estimates from two-point velocity increments. Less intermittency in rod tumbling computed from Jeffery's equation compared to rod tumbling from fully resolved rods in the flow further highlights the role of fluid motions at scales smaller than the rod length in generating extreme values of rod tumbling.

4. Conclusions

By tracking rods of different lengths in an isotropic turbulent flow, we study the effects and structure of turbulent fluid motions at different scales on slender rods. We find that the preferential alignment of rods with the directions of the perceived velocity gradient tensor changes with the rod length. In the dissipation range, there is a well-defined scale-independent preferred alignment where rods are most strongly aligned with the vorticity. In the inertial range, there is a different well-defined preferred alignment that is almost scale-independent where rods are most strongly aligned with the most extensional eigenvector of the strain-rate tensor.

In the inertial range, we find that the variances of both rod tumbling and rod stretching scale as $l^{-4/3}$, where l is the rod length. This scaling can be derived from the physical argument that rod tumbling and stretching are driven primarily by fluid motions of the same size as the rod length combined with K41 scaling relationships for the time scale of these turbulent fluid motions (see also Parsa & Voth 2014). A closer examination of the rod tumbling variance reveals that its value is higher than expected at transitional scales between the dissipation range and the inertial range (specifically, at $l \approx 60\eta$). By comparing rod tumbling data from different methods, we conclude that this is because fluid motions at scales smaller than l do not cancel out over the rod, but rather contribute to rod tumbling variance. For rod stretching statistics, we find that there is interesting behaviour at $l \approx 100\eta$. At this scale, the mean rod stretching relative to longitudinal fluid velocity increments shows a maximum and the skewness of rod stretching changes sign from being positive for rods in the tracer limit to becoming negative for rods well into the inertial range. Thus, the skewness of longitudinal velocity increments in the frame of rods in statistically steady alignment with the turbulent flow do not display scale independence in the inertial range; this is a marked contrast relative to longitudinal velocity increments taken in random orientations whose scale independence in the inertial range is predicted from Kolmogorov's 4/5 law.

The power-law scaling exponents of higher-order moments of rod tumbling and rod stretching show anomalous scaling as a consequence of turbulent intermittency. The scaling exponents for rod stretching compare well to scaling exponents for longitudinal

velocity increments in the flow and predictions from the refined similarity hypothesis (K62 theory). When the rod tumbling is computed from two-point transverse velocity increments across the rod length, the rod tumbling scaling exponents agree with the scaling exponents of transverse velocity increments in the flow. Together, this suggests that evaluating velocity increments in directions associated with fluid deformation does not seem to increase the departure of their scaling exponents from K41 theory predictions, though this departure is within the uncertainty limits of the data. However, if the rod tumbling is computed from fully resolved rod dynamics that take into account the fluid velocity variation along the full length of the rod, the scaling exponents do show a further departure from K41 theory predictions. This means that rod alignment does not necessarily cause rod dynamics to be more intermittent in comparison to structure functions in the inertial range, but that the effects of small-scale fluid motions on rod tumbling in combination with rod alignment does appear to result in additional intermittency.

Acknowledgements

REFERENCES

ALYONES, S. & BRUCE, C. W. 2015 Electromagnetic scattering and absorption by randomly oriented fibers. *J. Opt. Soc. Am.* A **32**, 1101–1108.

BATCHELOR, G. K. 1970 Slender-body theory for particles of arbitrary cross-section in Stokes flow. *J. Fluid Mech.* **44**, 419–440.

BORDOLOI, A. D. & VARIANO, E. A. 2017 Rotational kinematics of large cylindrical particles in turbulence. *J. Fluid Mech.* **815**, 199–222.

BYRON, M., EINARSSON, J., GUSTAVSSON, K., VOTH, G., MEHLIG, B. & VARIANO, E. 2015 Shape-dependence of particle rotation in isotropic turbulence. *Phys. Fluids* **27**, 035101.

CHEN, J., JIN, G. & ZHANG, J. 2015 Large eddy simulation of orientation and rotation of ellipsoidal particles in isotropic turbulent flows. *J. Turbul.* **17**, 308–326.

CHEN, S., SREENIVASAN, K. R., NELKIN, M. & CAO, N. 1997 Refined similarity hypothesis for transverse structure functions in fluid turbulence. *Phys. Rev. Lett.* **79**, 2253–2256.

CHERTKOV, M., PUMIR, A. & SHRAIMAN, B. I. 1999 Lagrangian tetrad dynamics and the phenomenology of turbulence. *Phys. Fluids* **11**, 2394–2410.

CHEVILLARD, L. & MENEVEAU, C. 2011 Lagrangian time correlations of vorticity alignments in isotropic turbulence: observations and model predictions. *Phys. Fluids* **23**, 101704.

CHEVILLARD, L. & MENEVEAU, C. 2013 Orientation dynamics of small, triaxial–ellipsoidal particles in isotropic turbulence. *J. Fluid Mech.* **737**, 571–596.

COX, R. G. 1970 The motion of long slender bodies in a viscous fluid. Part 1. General theory. *J. Fluid Mech.* **44**, 791–810.

DANISH, M. & MENEVEAU, C. 2018 Multiscale analysis of the invariants of the velocity gradient tensor in isotropic turbulence. *Phys. Rev. Fluids* **3**, 044604.

DAVIDSON, P. A. 2015 *Turbulence: An Introduction for Scientists and Engineers*. Oxford University Press.

DONZIS, D. A., YEUNG, P. K. & SREENIVASAN, K. R. 2008 Dissipation and enstrophy in isotropic turbulence: resolution effects and scaling in direct numerical simulations. *Phys. Fluids* **20**, 045108.

DUSENBERY, D. B. 2009 *Living at Micro Scale: The Unexpected Physics of Being Small*. Harvard University Press.

FRISCH, U. 1995 *Turbulence: The Legacy of A. N. Kolmogorov*. Cambridge University Press.

GIRIMAJI, S. S. & POPE, S. B. 1990 Material-element deformation in isotropic turbulence. *J. Fluid Mech.* **220**, 427–458.

GONZALEZ, O. & STUART, A. M. 2009 *A First Course in Continuum Mechanics*. Cambridge University Press.

GUALA, M., LUTHI, B., LIBERZON, A., TSINOBER, A. & KINZELBACH, W. 2005 On the evolution of material lines and vorticity in homogeneous turbulence. *J. Fluid Mech.* **533**, 1–21.

GUAZZELLI, É. & HINCH, J. 2011 Fluctuations and instability in sedimentation. *Annu. Rev. Fluid Mech.* **43**, 97–116.

GUSTAVSSON, K., EINARSSON, J. & MEHLIG, B. 2014 Tumbling of small axisymmetric particles in random and turbulent flows. *Phys. Rev. Fluids* **112**, 014501.

HAMLINGTON, P. E., SCHUMACHER, J. & DAHM, W. J. A. 2008 Direct assessment of vorticity alignment with local and nonlocal strain rates in turbulent flows. *Phys. Fluids* **20**, 111703.

HE, G.-W., RUBINSTEIN, R. & WANG, L.-P. 2002 Effects of subgrid-scale modeling on time correlations in large eddy simulation. *Phys. Fluids* **14**, 2186–2193.

ISHIHARA, T., GOTOH, T. & KANEDA, Y. 2009 Study of high-Reynolds number isotropic turbulence by direct numerical simulation. *Annu. Rev. Fluid Mech.* **41**, 165–180.

IYER, K. P., SREENIVASAN, K. R. & YEUNG, P. K. 2017 Reynolds number scaling of velocity increments in isotropic turbulence. *Phys. Rev. E* **95**, 021101.

JEFFERY, G. B. 1922 The motion of ellipsoidal particles immersed in a viscous fluid. *Proc. R. Soc. Lond.* A **102**, 161–179.

KHAYAT, R. E. & COX, R. G. 1989 Inertia effects on the motion of long slender bodies. *J. Fluid Mech.* **209**, 435–462.

KOLMOGOROV, A. N. 1941 Dissipation of energy in locally isotropic turbulence. *Dokl. Akad. Nauk SSSR* **32** (1), 16–18.

KOLMOGOROV, A. N. 1962 A refinement of previous hypotheses concerning the local structure of turbulence in a viscous incompressible fluid at high Reynolds number. *J. Fluid Mech.* **13**, 82–85.

KRAMEL, S., VOTH, G. A., TYMPEL, S. & TOSCHI, F. 2016 Preferential rotation of chiral dipoles in isotropic turbulence. *Phys. Rev. Lett.* **117**, 154501.

LEUNG, T., SWAMINATHAN, N. & DAVIDSON, P. A. 2012 Geometry and interaction of structures in homogeneous isotropic turbulence. *J. Fluid Mech.* **710**, 453–481.

LI, Y. & MENEVEAU, C. 2005 Origin of non-Gaussian statistics in hydrodynamic turbulence. *Phys. Rev. Lett.* **95**, 164502.

LI, Y., PERLMAN, E., WAN, M., YANG, Y., MENEVEAU, C., BURNS, R., CHEN, S., SZALAY, A. & EYINK, G. 2008 A public turbulence database cluster and applications to study Lagrangian evolution of velocity increments in turbulence. *J. Turbul.* **9**, N31.

LI, Y. I. & MENEVEAU, C. 2006 Intermittency trends and Lagrangian evolution of non-Gaussian statistics in turbulent flow and scalar transport. *J. Fluid Mech.* **558**, 133–142.

LOPEZ, D. & GUAZZELLI, É. 2017 Inertial effects on fibers settling in a vortical flow. *Phys. Rev. Fluids* **2**, 024306.

LUND, T. S. & ROGERS, M. M. 1994 An improved measure of strain state probability in turbulent flows. *Phys. Fluids* **6**, 1838–1847.

LUNDELL, F., SÖDERBERG, L. D. & ALFREDSSON, P. H. 2011 Fluid mechanics of papermaking. *Annu. Rev. Fluid Mech.* **43**, 195–217.

LUTHI, B., OTT, S., BERG, J. & MANN, J. 2007 Lagrangian multi-particle statistics. *J. Turbul.* **8**, N45.

LUTHI, B., TSINOBER, A. & KINZELBACH, W. 2005 Lagrangian measurement of vorticity dynamics in turbulent flow. *J. Fluid Mech.* **528**, 87–118.

MARHEINEKE, N. & WEGENER, R. 2006 Fiber dynamics in turbulent flows: general modeling framework. *SIAM J. Appl. Maths* **66**, 1703–1726.

MENEVEAU, C. & KATZ, J. 2000 Scale-invariance and turbulence models for large-eddy simulation. *Annu. Rev. Fluid Mech.* **32**, 1–32.

MENEVEAU, C. & SREENIVASAN, K. R. 1991 The multifractal nature of turbulent energy dissipation. *J. Fluid Mech.* **224**, 429–484.

NASO, A. & PUMIR, A. 2005 Scale dependence of the coarse-grained velocity derivative tensor structure in turbulence. *Phys. Rev.* E **72**, 056318.

NELKIN, M. 1999 Enstrophy and dissipation must have the same scaling exponent in the high Reynolds number limit of fluid turbulence. *Phys. Fluids* **11**, 2202–2204.

NEWSOM, R. K. & BRUCE, C. W. 1994 The dynamics of fibrous aerosols in a quiescent atmosphere. *Phys. Fluids* **6**, 521–530.

NEWSOM, R. K. & BRUCE, C. W. 1998 Orientational properties of fibrous aerosols in atmospheric turbulence. *J. Aerosol. Sci.* **29**, 773–797.

NI, R., KRAMEL, S., OUELLETTE, N. T. & VOTH, G. A. 2015 Measurements of the coupling between the tumbling of rods and the velocity gradient tensor in turbulence. *J. Fluid Mech.* **766**, 202–225.

NI, R., OUELLETTE, N. T. & VOTH, G. A. 2014 Alignment of vorticity and rods with Lagrangian fluid stretching in turbulence. *J. Fluid Mech.* **743**, R3.

NIAZI, A. M., SARDINA, G., BRANDT, L., KARP-BOSS, L., BEARON, R. N. & VARIANO, E. A. 2017 Sedimentation of inertia-less prolate spheroids in homogenous isotropic turbulence with application to non-motile phytoplankton. *J. Fluid Mech.* **831**, 655–674.

OBOUKHOV, A. M. 1962 Some specific features of atmospheric tubulence. *J. Fluid Mech.* **13**, 77–81.

OLSON, J. A. & KEREKES, R. J. 1998 The motion of fibres in turbulent flow. *J. Fluid Mech.* **377**, 47–64.

PARSA, S., CALZAVARINI, E., TOSCHI, F. & VOTH, G. A. 2012 Rotation rate of rods in turbulent fluid flow. *Phys. Rev. Lett.* **109**, 134501.

PARSA, S. & VOTH, G. A. 2014 Inertial range scaling in rotations of long rods in turbulence. *Phys. Rev. Lett.* **112**, 024501.

PERLMAN, E., BURNS, R., LI, Y. & MENEVEAU, C. 2007 Data exploration of turbulence simulations using a database cluster. In *Supercomputing SC07*. ACM, IEEE.

POPE, S. B. 2000 *Turbulent Flows*. Cambridge University Press.

PRUPPACHER, H. R. & KLETT, J. D. 2012 *Microphysics of Clouds and Precipitation*. Springer.

PUJARA, N., OEHMKE, T. B., BORDOLOI, A. D. & VARIANO, E. A. 2018 Rotations of large inertial cubes, cuboids, cones, and cylinders in turbulence. *Phys. Rev. Fluids* **3**, 054605.

PUJARA, N. & VARIANO, E. A. 2017 Rotations of small, inertialess triaxial ellipsoids in isotropic turbulence. *J. Fluid Mech.* **821**, 517–538.

PUMIR, A., BODENSCHATZ, E. & XU, H. 2013 Tetrahedron deformation and alignment of perceived vorticity and strain in a turbulent flow. *Phys. Fluids* **25**, 035101.

PUMIR, A. & WILKINSON, M. 2011 Orientation statistics of small particles in turbulence. *New J. Phys.* **13**, 093030.

RAVNIK, J., MARCHIOLI, C. & SOLDATI, A. 2017 Application limits of Jeffery's theory for elongated particle torques in turbulence: a DNS assessment. *Acta Mechanica* **229**, 827–839.

SHIN, M. & KOCH, D. L. 2005 Rotational and translational dispersion of fibres in isotropic turbulent flows. *J. Fluid Mech.* **540**, 143–173.

SINHUBER, M., BEWLEY, G. P. & BODENSCHATZ, E. 2017 Dissipative effects on inertial-range statistics at high Reynolds numbers. *Phys. Rev. Lett.* **119**, 134502.

SPURNY, K. 2000 Atmospheric contamination by fibrous aerosols. In *Aerosol Chemical Processes in the Environment*. chap. 26, Lewis Publishers.

SREENIVASAN, K. R. & ANTONIA, R. A. 1997 The phenomenology of small-scale turbulence. *Annu. Rev. Fluid Mech.* **29**, 435–472.

SUBRAMANIAN, G. & KOCK, D. L. 2005 Inertial effects on fibre motion in simple shear flow. *J. Fluid Mech.* **535**, 383–414.

VOTH, G. A. & SOLDATI, A. 2017 Anisotropic particles in turbulence. *Annu. Rev. Fluid Mech.* **49**, 249–276.

XU, H., PUMIR, A. & BODENSCHATZ, E. 2011 The Pirouette effect in turbulent flows. *Nat. Phys.* **7**, 709–712.

YANG, Y., HE, G.-W. & WANG, L.-P. 2008 Effects of subgrid-scale modeling on Lagrangian statistics in large-eddy simulation. *J. Turbul.* **9**, N8.

YU, H., KANOV, K., PERLMAN, E., GRAHAM, J., FREDERIX, E., BURNS, R., SZALAY, A., EYINK, G. & MENEVEAU, C. 2012 Studying Lagrangian dynamics of turbulence using on-demand fluid particle tracking in a public turbulence database. *J. Turbul.* **13**, N12.